Supplementary information:

Single crystals of electrically conductive 2D MOFs: structural and electrical transport properties

Robert W. Day[1], D. Kwabena Bediako[2,3], Mehdi Rezaee[4], Lucas R. Parent[5,6], Grigorii Skorupskii[1], Maxx Q. Arguilla[1], Christopher H. Hendon[7], Ivo Stassen[1], Nathan C. Gianneschi[5], Philip Kim[2], and Mircea Dincă[1]*

[1]Department of Chemistry, Massachusetts Institute of Technology, Cambridge, Massachusetts 02138, USA.

[2]Department of Physics, Harvard University, Cambridge, Massachusetts 02138, USA.

[3]Department of Chemistry, University of California Berkeley, Berkeley, California 94720, USA

[4]John A. Paulson School of Engineering and Applied Sciences, Harvard University, Cambridge, Massachusetts 02138, USA.

[5]Department of Chemistry, Materials Science & Engineering, Biomedical Engineering, International Institute for Nanotechnology, Northwestern University, Evanston, Illinois 60208, USA.

[6]Innovation Partnership Building, University of Connecticut, Storrs, CT 06269, USA.

[7]Department of Chemistry and Biochemistry, University of Oregon, Eugene, OR 97401, USA.

*email: mdinca@mit.edu

Materials

Starting materials were purchased from Sigma-Aldrich or TCI and used without further purification. 2,3,6,7,10,11-hexaaminotriphenylene hexahydrochloride, HATP·6HCl, was prepared according to a procedure published elsewhere.[1] No unexpected or unusually high safety hazards were encountered.

Methods

Synthesis:

$Ni_3(HITP)_2$ rods

A solution of 4 mg (0.017 mmol) of nickel chloride hexahydrate ($NiCl_2$ $6H_2O$) in 3 mL of water was added to a solution of 3 mg (0.006 mmol) of HATP 6HCl in 3 mL of water, and heated at 60 °C. To this was added a solution of 75 mg (0.914 mmol) of sodium acetate in 3 ml water. This mixture was heated in an open vial for 2 hours at 60 °C. The resulting black powder was centrifuged, and washed in water, ethanol and acetone twice each.

$Cu_3(HHTP)_2$ rods

1.5 ml water was added to a 20 ml glass vial containing 7.8 mg (0.039 mmol) of copper acetate hydrate ($Cu_2(OAc)_4$ H_2O) and 7 mg (0.022 mmol) of HHTP, which was sonicated for 5 mins. 0.15 ml DMF was then added dropwise to this mixture followed by 5 mins of sonication. The capped vial was heated at 80 ºC for 6 hours. The resulting blue powder was centrifuged, and washed in water, ethanol and acetone twice each.

$Cu_3(HHTP)_2$ particles

233 mg (0.718 mmol) of HHTP was dissolved in 3 ml DMF and 24 ml H_2O in a 100 ml glass jar. Separately, 410 mg (1.64 mol) of copper sulfate pentahydrate ($CuSO_4$ $5H_2O$) was dissolved in 9 ml H_2O. Both solutions were heated at 80 ºC in an oven for 5 minutes, at which point they were mixed and heated for 12 hours. The resulting blue powder was centrifuged, and washed in water, ethanol and acetone twice each.

Exfoliation of $Cu_3(HHTP)_2$ particles to obtain flakes

40 mg of washed $Cu_3(HHTP)_2$ particles were placed in a 20 ml glass vial. To this was added either 10 ml's of isopropanol, DI water, acetonitrile, or n-methylpyrrolidone, which were sonicated for 1-2 hours in a bath. Samples were centrifuged for 10 minutes, and the flakes were obtained by isolating the blue supernatant.

TEM

TEM Sample Preparation: TEM grids of the 3 samples ($Ni_3(HITP)_2$ rods, $Cu_3(HHTP)_2$ rods, and exfoliated $Cu_3(HHTP)_2$) were prepared by drop-casting 3.5 µL of the respective sample solution onto [Cu-mesh] lacey-C substrate grids (Electron Microscopy Sciences, Hatfield, PA). The droplets of sample were allowed to sit on the grids in ambient conditions for ~20-30s, and were then wicked dry with filter paper. The prepared TEM grids were then stored in a desiccator until they were used for TEM characterization.

TEM Characterization: TEM imaging was performed using a JEOL (JEOL Ltd., Tokyo, Japan) GrandARM 300 operating at 300 keV (cold field emission gun) equipped with a Gatan (Roper Technologies, Sarasota, FL) OneView IS (CMOS electron sensor) detector. Microscope operating conditions for TEM imaging: FEG emission: 15 µA, spot size 4, #2 µm CL(1) aperture, #1 µm OL(upper) aperture. The GrandARM 300 was aligned for low-dose imaging, and the precise electron beam current (0.94 nA for the operating conditions used here) was previously measured and calibrated using a faraday cup. The beam diameter used for HRTEM imaging was measured at all magnifications used, enabling accurate calculation of dose rate and cumulative dose per image. The TEM dose rate was maintained between 4.8 $e^-/Å^2s$ and 18.7 $e^-/Å^2s$. We note that no damage to the MOF structures were detected during brief exposures at these dose conditions, but higher doses would cause significant and rapid structural damage. HRTEM images were acquired using Gatan DigitalMicrograph GMS software at 0.3 s exposure time (~1.5 – 5.6 $e^-/Å^2$ cumulative dose per image), with focusing done adjacent to the region imaged to minimize beam exposure prior to image acquisition (standard low dose imaging protocols).

TEM Data Analysis: Analysis of the raw HRTEM data (.dm4), including FFT and intensity profile analysis, was done using FIJI ImageJ software (https://imagej.net/Fiji/).[1]

Synchrotron PXRD of $Cu_3(HHTP)_2$

High resolution synchrotron powder diffraction data were collected using the mail-in service of the beamline 11-BM at the Advanced Photon Source (APS), Argonne National Laboratory using an average wavelength of 0.414560 Å. Discrete detectors covering an angular range from -6 to 16 º 2θ are scanned over a 34º 2θ range, with data points collected every 0.001º 2θ and scan speed of 0.01º/s. The 11-BM instrument uses x-ray optics with two platinum-striped mirrors and a double-crystal Si(111) monochromator, where the second crystal has an adjustable sagittal bend. Ion chambers monitor incident flux. A vertical Huber 480 goniometer, equipped with a Heidenhain encoder, positions an analyzer system comprised of twelve perfect Si(111) analyzers and twelve Oxford-Danfysik $LaCl_3$ scintillators, with a spacing of 2º 2θ. Analyzer orientation can be adjusted individually on two axes. A three-axis translation stage holds the sample mounting and allows it to be spun, typically at ~5400 RPM (90 Hz). A Mitsubishi robotic arm is used to mount and dismount samples on the diffractometer. Oxford Cryosystems Cryostream Plus device allows sample temperatures to be controlled over the range 80-500 K when the robot is used. The diffractometer is controlled via EPICS. Data are

collected while continually scanning the diffractometer 2θ arm. A mixture of NIST standard reference materials, Si (SRM 640c) and Al_2O_3 (SRM 676) is used to calibrate the instrument, where the Si lattice constant determines the wavelength for each detector. Corrections are applied for detector sensitivity, 2θ offset, small differences in wavelength between detectors, and the source intensity, as noted by the ion chamber before merging the data into a single set of intensities evenly spaced in 2θ.

The washed powder of $Cu_3(HHTP)_2$ was dried under dynamic vacuum at room temperature, and packed in air into a Kapton capillary provided by 11-BM. The PXRD pattern was then collected at 295 K. The pattern was indexed in TOPAS-Academic, giving the best fits to the space group *C*2 (5) and its extinction equivalents. The structural model was then built based on the obtained unit cell in Materials Studio by changing the stacking of a DFT-optimized structure used in prior work by our group. The PXRD pattern was then fitted with the unit cell parameters of the produced model, using Pawley refinement as implemented in TOPAS-Academic. Significant broadening was observed for the *(0kl)* and *(00l)*, and was corrected for as anisotropic strain broadening according to the model by Stephens et al. for a monoclinic unit cell. The results of the refinement are presented in the Table.

Device fabrication: Samples of rods, or flakes were suspended in ethanol and dropcast onto Si substrates having pre-patterned marks for optical alignment and registration. 2 layers of MMA and 1 layer of PMMA were coated onto the chips, where the layers were baked at 85 C for 5 minutes in a vacuum oven. Electron beam lithography at 30 kV was used to pattern contacts, and 3 nm Ti/ 250 nm Pd were evaporated using an electron beam evaporator.

Growth Discussion: With an understanding of the conductive 2D MOF's structure, we discuss key synthetic observations. First, the growth of larger, isolated crystals is not trivial as many attempts lead to the formation of non-crystalline material or impurities. Second, the tendency to form small or interconnected crystals may indicate fast nucleation rates and/or poor reversibility for crystal growth, which are consistent with the strong metal-ligand bonds known for metal-semiquinone/diimine systems as well as the poor solubility and thus high supersaturation of the ligand in water. Third, the tendency to form rods indicates that out-of-plane stacking predominates over in-plane metal-ligand layer formation, and the rod morphology increases the interaction of the solvent with the metals/hydrophilic ends of the ligand at the surface of the rod's cross section and minimizes that for the ligand's hydrophobic triphenylene core. Our use of copper sulfate (sodium acetate) over copper acetate (NH_4OH) for $Cu_3(HHTP)_2$ growth ($Ni_3(HITP)_2$) yielded larger, isolated crystals, which is consistent with a weaker base reducing nucleation rates and increasing reversibility of the metal-ligand bond. Additionally, increasing the temperature alone yields larger in-plane dimensions for $Cu_3(HHTP)_2$ crystals, consistent with higher temperatures increasing the solubility/decreasing the supersaturation of the ligand, as well as increasing the reversibility of the M-L bond. Fourth, we note that, phenomenologically, the rate of oxidation of the ligand as well as solvent choice appear to be critical parameters that merit further investigation. In the absence of air, we have not obtained $Ni_3(HITP)_2$, and scaling up requires air bubbling;

however, heating the HATP ligand in air without metal and base for a few minutes, leads to a pink color and consequently small to no MOF crystals. For some $Cu_3(HHTP)_2$ syntheses, we observe a yellow supernatant that upon removal from its closed container after growth changes to blue following additional heating in air, potentially indicating that some growths may be limited by O_2. Furthermore, we obtain our largest crystals in solutions that are entirely water or with a small amount (~10%) of cosolvent. Increasing the amount of cosolvent in water leads to smaller or no MOF crystals. We note the solubility of dissolved O_2, and its rate of transfer, in water can be orders of magnitude less than in organic solvents, and decreases with temperature. Given the poor solubility of the ligand, water may also help promote the 2D layer structure by promoting ligand stacking. Together, these results suggest that larger isolated crystals may be obtained by further reducing nucleation rates, by promoting the reversibility of the M-L bonds and the ligand stacking, and by controlling the rate and total amount of ligand oxidation.

Device Discussion: Literature precedence and additional data are consistent with our interpretation of metallicity or degenerate doping in $Ni_3(HITP)_2$. First, previously reported band structures computed by density functional theory (DFT), as well as our own calculations (Supplementary Figure 3) predict the Fermi level to lie within bands for both in-plane and out-of-plane transport. Second, it has been shown phenomenologically that various metallic systems, including disordered transition metal alloys, conductive polymers, and carbon nanotubes, can show a weak but positive conductance dependence on temperature when the conductivity is less than a certain threshold value.[2] Third, doped organic polymers systems that are metallic have similar reduced activation energy values and slopes in their Zabrodskii plots, and similar conductivity values to our $Ni_3(HITP)_2$ devices.[3] For example, for the device in Fig. 2a, we estimate the 4-probe (2-probe) conductivity to be 142 S/cm (40 S/cm) for a resistance value of 415 Ω (8.6 kΩ), a channel length of 165 nm (955 nm) and diameter of 188 nm as determined from SEM images (Supplementary Figure 4). Other devices yielded conductivities of 148, 104, 102, and 95 S/cm, which are in line with conductivity values for some metallic polymer systems. Fourth, we observe low contact resistance and linear I-V curves (Fig. 2b) down to our lowest temperatures, which would not be expected for a semiconductor. Last, the reversibility of conductance with magnetic field and the reversibility of the magnetoconductance's temperature dependence (Fig. 2b, inset) indicate that neither electrical drift nor poor heat transfer are responsible for our observed conductivity changes or lack thereof.

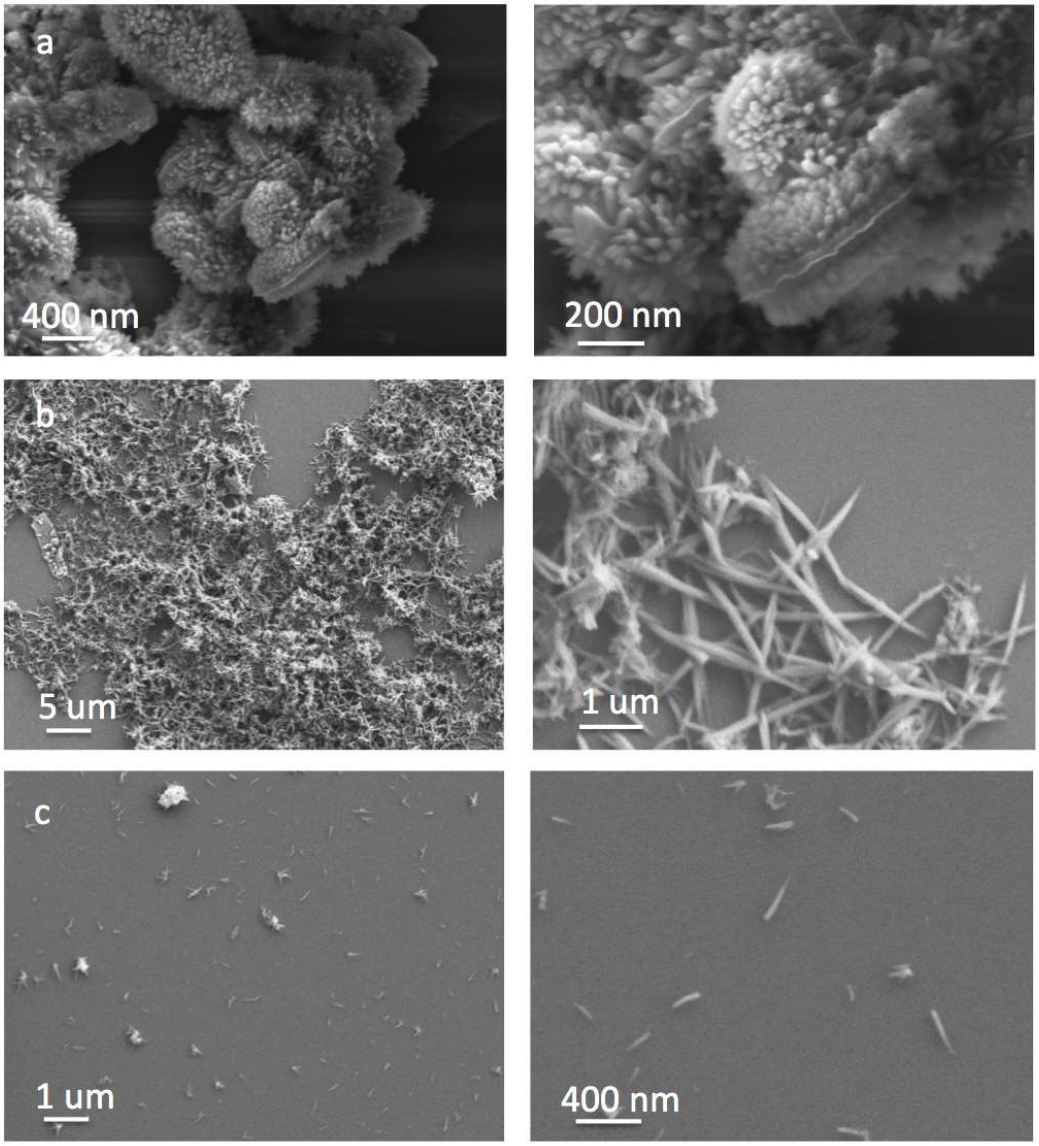

Supplementary figure 1 - Growth of $Ni_3(HITP)_2$: interconnected morphology using published conditions (a) and isolated rods using new conditions (b and c)

SEM images of morphology observed following growth of $Ni_3(HITP)_2$ using previously reported conditions (a), using new conditions with $NiCl_2$ and sodium acetate in an open vial (b), and using a 10X higher concentration of sodium acetate with nickel nitrate in a closed vial (c). The use of NH_4OH generally yielded $Ni_3(HITP)_2$ morphologies that were difficult to isolate individual crystals from as the crystals appear to emanate from a shared base. The use of sodium acetate led to isolated rods in appreciably higher yields and were used for TEM and device fabrication.

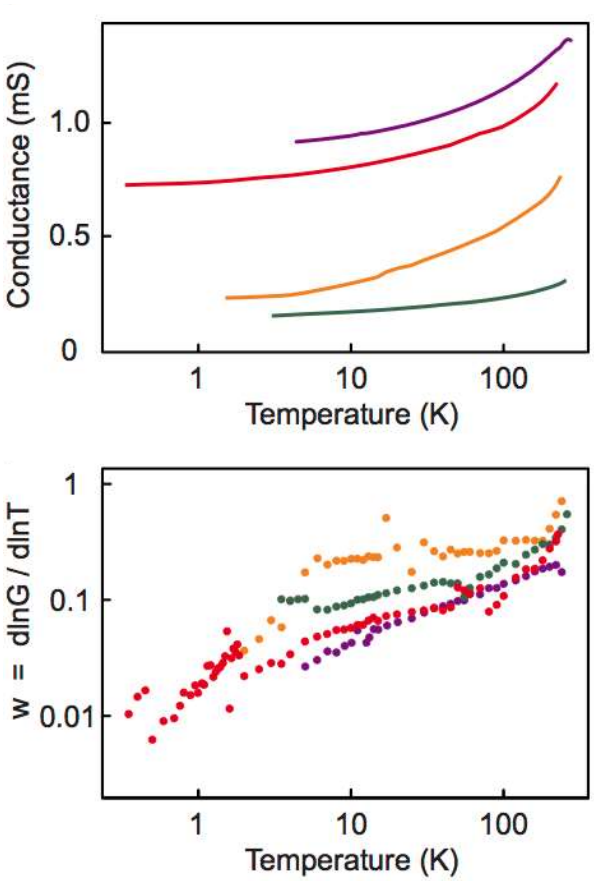

Supplementary figure 2 - $Ni_3(HITP)_2$ rod devices and variable temperature (VT) conductivity measurements. Top, Temperature dependent conductance traces for four $Ni_3(HITP)_2$ devices. **Bottom,** Zabrodskii plot showing reduced activation energy (w) as a function of temperature for the four traces.

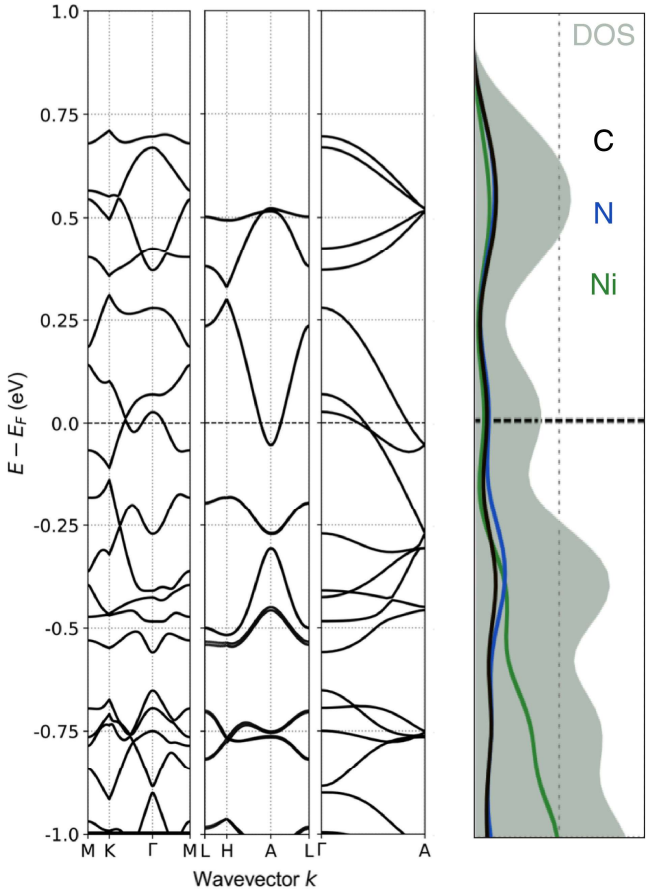

Supplementary figure 3 – Band structure and DOS for NiHITP

Calculated band structure of NiHITP from DFT calculations and density of states for Γ to A. Beginning with the experimental crystal structure the material was geometrically equilibrated in VASP using the PBEsol functional, with a 500 eV cutoff, and a 2 x 2 x 4 k-grid. The electronic band structure was then computed using the HSE06 functional, sampling explicit k-paths. The Fermi level crosses the band for the Γ to A direction, which is the orientation of the rod devices and consistent with the observed metallic behavior. Density of states calculation suggest that C, Ni, and N all contribute to these bands.

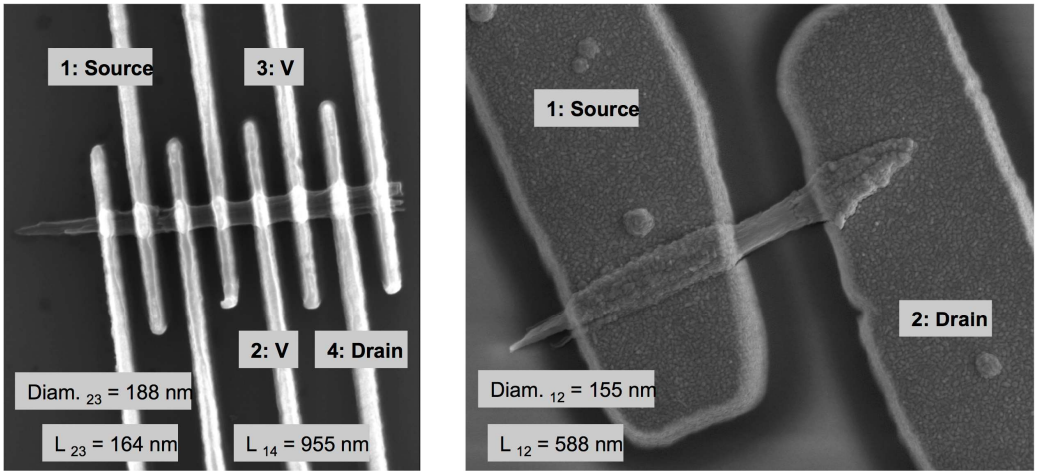

Supplementary figure 4– Estimation of conductivity values

Left, Plan-view SEM image for the device in Figure 2a. **Right,** Plan view SEM of a second device.

For four-probe measurements, conductivity was calculated using the four-probe resistance (R_{23}) measured across a channel length having a circular cross-section. The diameter (D_{23}) and length of the channel (L_{23}) were determined by SEM with the length being measured from edge to edge of the contacts. R_{23} was calculated by dividing the measured voltage (V_{23}) by the applied current ($I_{sd} = I_{14}$). For this device, we measured V_{23} = 42 uV and I_{14} = 100 nA for an R_{23} of 415 Ω, L_{23} = 164 nm, and D_{23} = 188 nm for a conductivity of 142 S/cm. The two probe conductivity is estimated as 40 S/cm for a two-probe resistance (R_{14}) of 8.6 kΩ, and channel length (L_{14}) of 955 nm. L_{14} is the distance from the edge of contact 1 to the edge of contact 4, and subtracting the widths of the 4 metal contacts between contact 1 and 4.

For a second two-probe device (right), we estimate a conductivity of 104 S/cm for a resistance of 3 kΩ, a diameter of 155 nm, and channel length of 588 nm.

For a third device, we estimate a conductivity of 148 S/cm for a resistance of 787 Ω, a diameter of 150 nm, and channel length of 206 nm.

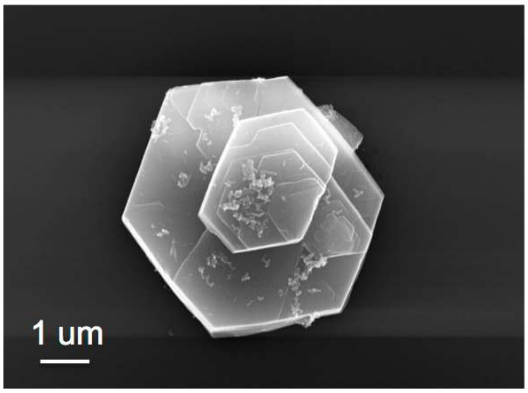

Supplementary figure 5 - Growth of $Cu_3(HHTP)_2$ particles. Particles with six-sided cross sections were obtained with widths up to 5 ums.

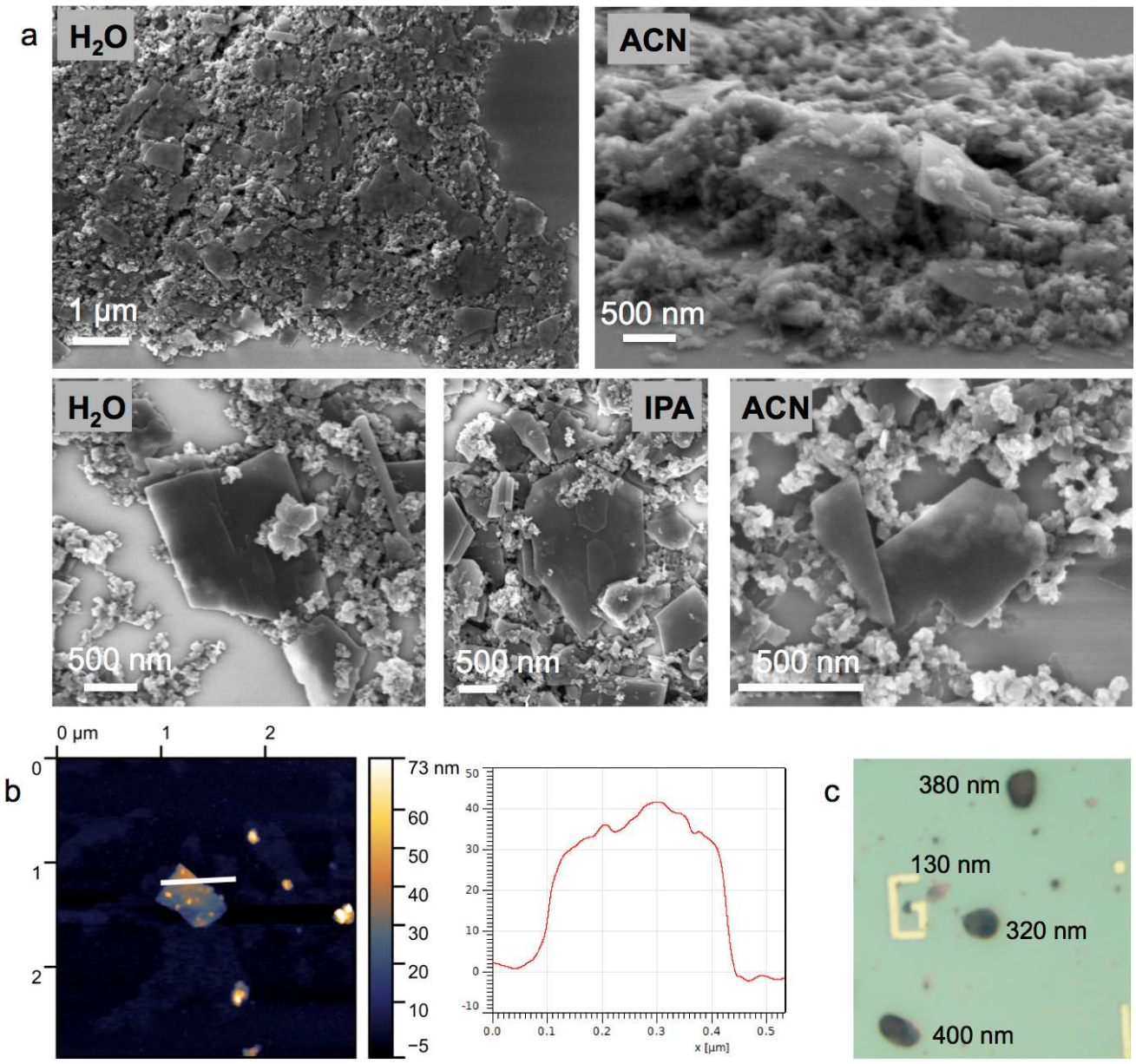

Supplementary figure 6 – Exfoliation of $Cu_3(HHTP)_2$ flakes

a, SEM images of exfoliated samples using different solvents. **b,** 2D AFM scan and height profile from white line. **c,** Bright-field optical image of exfoliated $Cu_3(HHTP)_2$ flakes and their corresponding heights as determined from AFM. For exfolitation, $Cu_3(HHTP)_2$ was sonicated for 1-2 hours in acetonitrile, water, isopropanol, or n-methylpyrrolidone. The top-left image illustrates the concentration and dimensions of flakes for a representative process with water. Top-right is an angled perspective showing the thin flakes on top of small particles. Bottom-right, middle and left images were obtained after sonication in water, isopropanol, and acetonitrile respectively. N-methylpyrrolidone resulted in a brown supernatant and presumably dissolved the MOF.

Supplementary figure 7 – Single crystal measurements of $Cu_3(HHTP)_2$

Device	Resistance (ohm)	Conductivity (S/cm)	Channel width (nm)	Channel height (nm)	Channel length (nm)
Rod 1	$5.62 * 10^5$	1.5	111	111	822
Rod 2	$5.7 * 10^5$	1.93	124	124	1329
Rod 3	$1.26 * 10^6$	0.64	154	154	1508
Flake 1	$1.3 * 10^5$	0.57	916	315	2137
Flake 2	$8.4 * 10^4$	0.52	2849	200	2508

Table showing parameters for different devices and their corresponding conductivities. Resistances were determined by a sourcemeter by measuring the current at a given applied voltage. Channel widths, heights and lengths were measured using an SEM. For rods, an approximately circular cross section was assumed whose channel width equals the channels height.

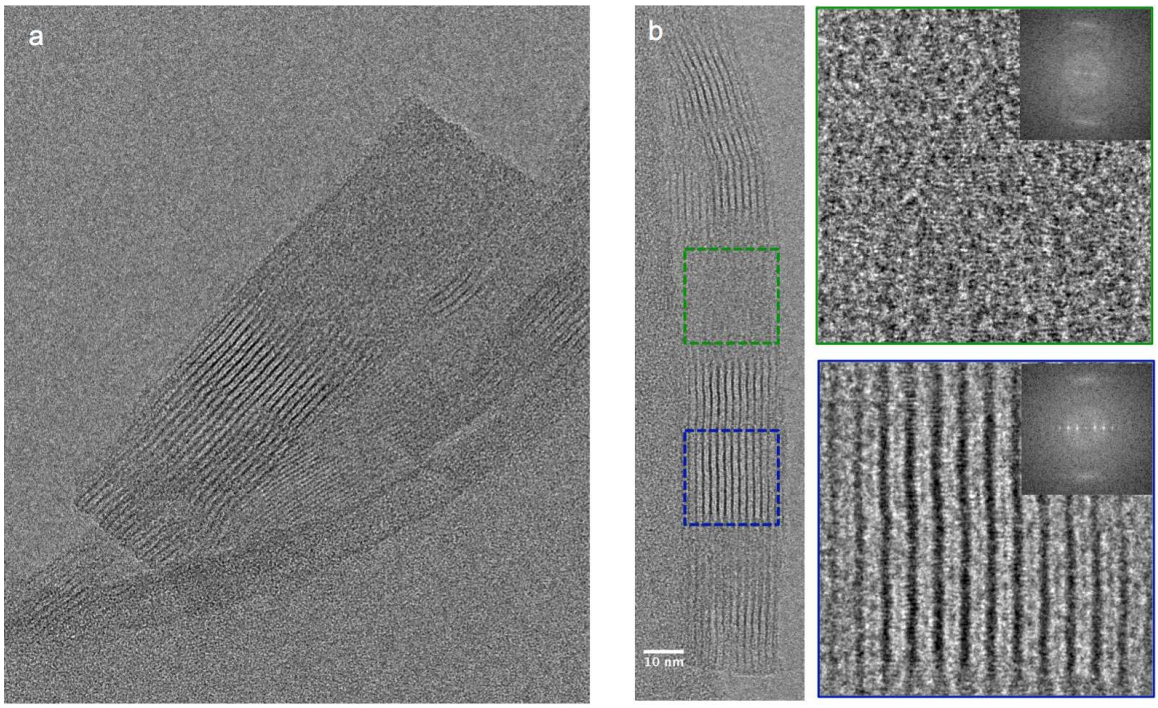

Supplementary figure 8 – TEM and FFT of $Ni_3(HITP)_2$ rods

a, A low magnification image of the $Ni_3(HITP)_2$ rod from Figure 4a. **b,** Low (left) and high-magnification (right, top and bottom) image of a different $Ni_3(HITP)_2$ rod. The high-magnification image (blue, right) and FFT (inset) are consistent with our assigned zone axis in figure 4. We note that some regions of these rods, such as the area in the green box, do not show strong contrast fringes. An FFT of the region in green (right top, inset) shows spots at ~ 0.33 nm, indicating that the layers are ordered with a similar orientation to that in the blue box. Contrast fringes both above the green box and below the blue box appear to lie along the same lines as the contrast lines within the blue box, suggesting that some coherency exists over that length. This would be consistent with a stacking fault being present between the blue and green boxes that maintains pore continuity but which rotates the crystal out of a high-contrast zone-axis. We observe similar regions for $Cu_3(HHTP)_2$ rods in supplementary figure 9. An alternative possibility is that the aligned layers shift at some point after growth, although we note this is less likely given that the edges of the rod also appear continuous and parallel over this same length.

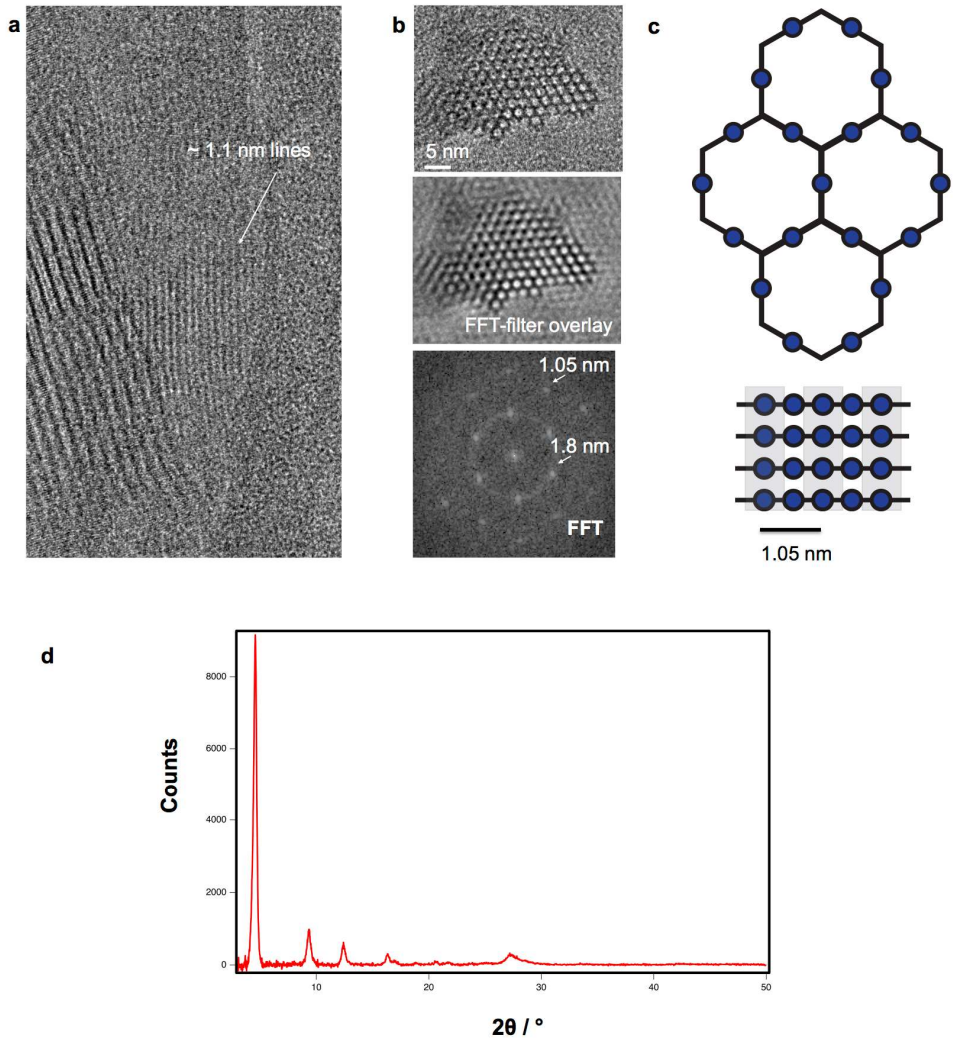

Supplementary figure 9 – Two additional zone axes of $Ni_3(HITP)_2$ and PXRD

a, TEM image of a zone axis with fringes of ~ 1.1. nm. **b**, TEM of a honeycomb lattice, an FFT-filtered overlay and FFT of the honeycomb lattice, showing 1.05 nm and 1.8 nm features. **c,** Structural model rotated 90° from schematic in Figure 4a. The zone axis in Figure 4a plus these two zone axes are consistent with viewing the eclipsed, or near-eclipsed, stacking structure along three orthogonal directions. **d,** PXRD pattern of samples used for TEM images and devices.

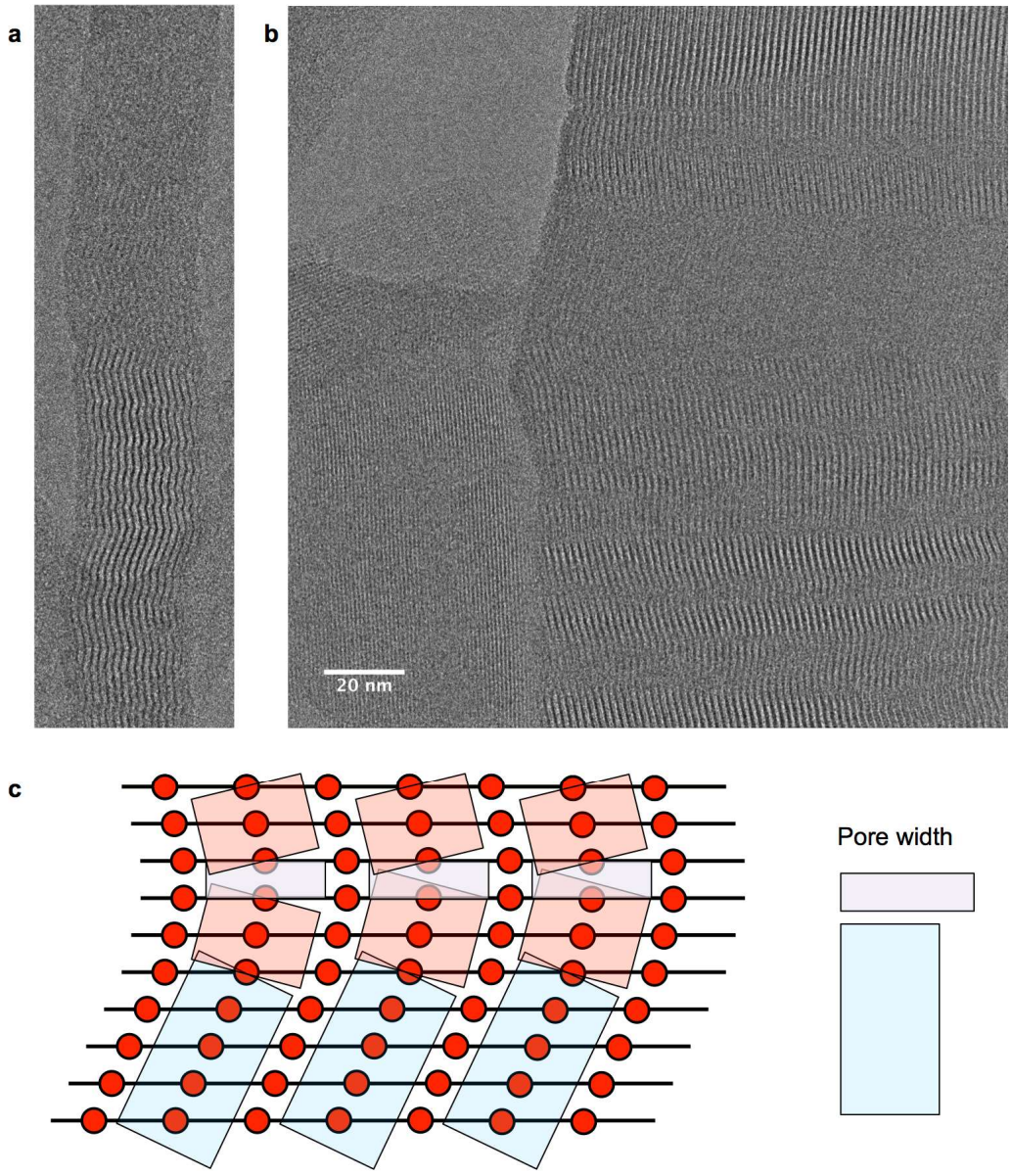

Supplementary figure 10 – TEM of $Cu_3(HHTP)_2$ rods and layer stacking

a, Low-magnification image for TEM image and FFT in figure 4b. **b,** Low-magnification image for two additional $Cu_3(HHTP)_2$ rods. **c,** Schematic illustrating 2D layer stacking and pore width. For the rod on the left in b, we see a zone-axis with ~ 1.1 nm spaced fringes consistent with our model but viewed from a different perspective (i.e. rotated 90 from schematic in top of figure 4c), similar to supplementary figure 8,c with $Ni_3(HITP)_2$. For the rod on the right in b, high-contrast zone axes can be separated by lower-contrast areas, consistent with stacking faults that can rotate the lattice into lower contrast zone axes when viewed from the same perspective. Similar features are seen for $Ni_3(HITP)_2$ in supplementary figure 4. Schematic in c shows how variation in layer stacking offset can lead to different pore widths, and different angles between the layers and the pores as seen in the FFT in figure 4b.

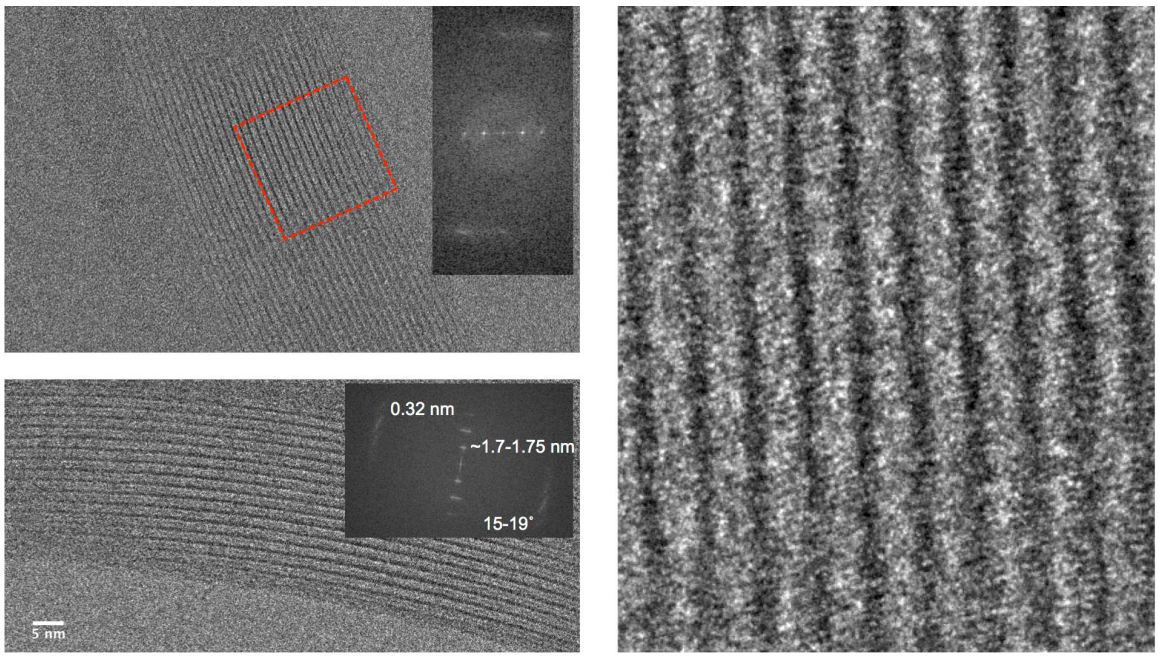

Supplementary figure 11 - TEM and FFTs of additional $Cu_3(HHTP)_2$ rods

TEM images and FFTs from three different $Cu_3(HHTP)_2$ rods showing that the 2D layers are not perpendicular to the pores.

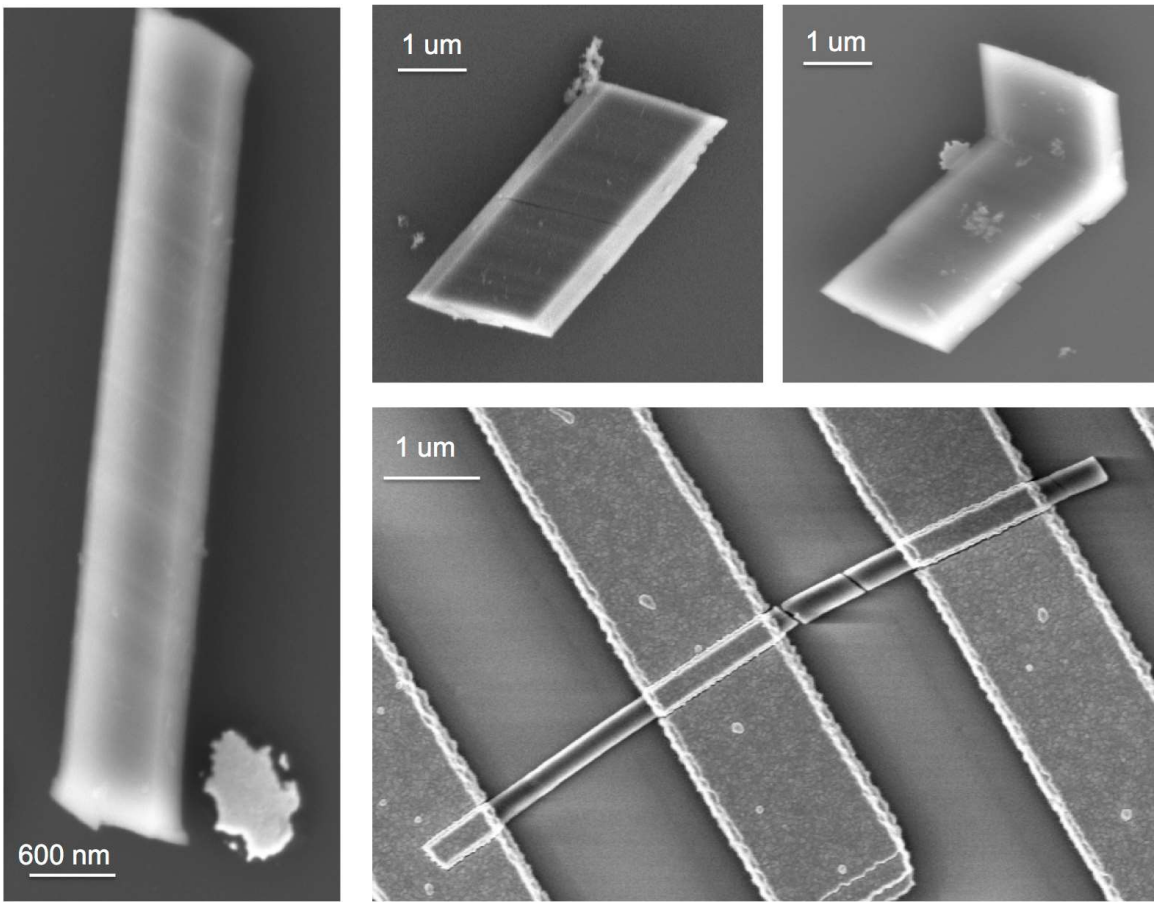

Supplementary figure 12 – Morphology of $Cu_3(HHTP)_2$ crystals

Plan-view SEM images of $Cu_3(HHTP)_2$ crystals, showing that contrast features and end facets are not perpendicular to the rod's long axis, consistent with a structural model where the layers are not perpendicular to the pores. The kink seen in the top right image may arise from a single stacking fault. Bottom right shows a broken rod that was part of a device, and shows commonly observed breaks that occur at angles similar to the end facets and contrast features.

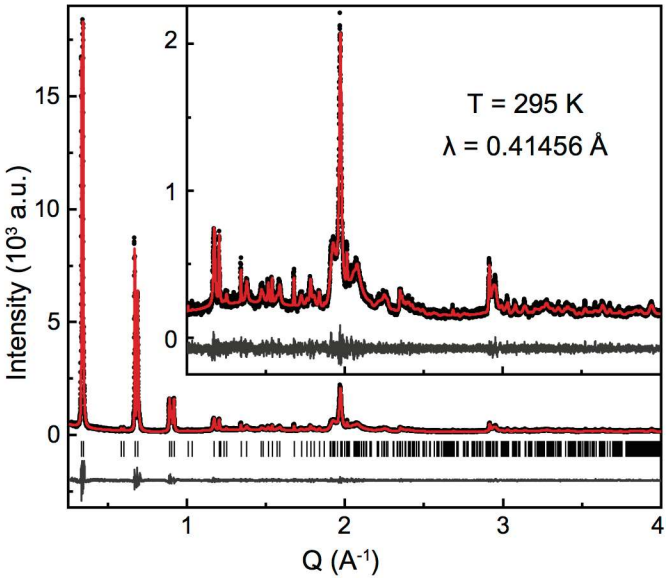

Supplementary figure 13 – Synchrotron PXRD of CuHHTP

The synchrotron powder X-ray diffraction pattern provides evidence for the structure observed by TEM, where the layers are not normal to the pores, and confirmed that the bulk material was single-phase. A Pawley refinement of the pattern yielded a monoclinic C-centered cell (a = 20.87 Å, b = 37.42 Å, c = 3.30 Å, β = 87.22). While the data quality was insufficient for a Rietveld refinement, the metric parameters of the unit cell allowed us to propose a structural model very similar to the one proposed from the TEM study. Here, the 2D layers of the overall formula $Cu_3(HHTP)_2$ stack with a constant shift of 0.9 Å in the hexagonal plane, resulting in an effective 15 deg. tilt of the stacking axis. The layered structure of the material can explain the observed strong anisotropy of the peak widths in the PXRD pattern. The strongly broadened peaks belong to either the (00l) or the (0kl) sets, which are both heavily dependent on the stacking shift in our proposed model. At the same time, the (hk0) and the (h0l) sets, which should be largely independent of the stacking shift, remain sharp.

Table S1. Results of the Pawley refinement of the synchrotron PXRD pattern for $Cu_3(HHTP)_2$. For R_{wp} and R_p the background-subtracted values are provided.

$Cu_3(HHTP)_2$ (295 K)	
Space group	*C*2/m (12)
a (Å)	20.87
b (Å)	37.42
c (Å)	3.30
β (°)	87.22
Unit cell volume (Å³)	2573
R_{wp} (%)	5.23
R_p (%)	6.09
GoF	1.16

Supplementary References

1. Chen, L. *et al.* Noncovalently Netted, Photoconductive Sheets with Extremely High Carrier Mobility and Conduction Anisotropy from Triphenylene-Fused Metal Trigon Conjugates *J. Am. Chem. Soc.* **131**, 7287 (2009).
2. Ahlskog, M., Reghu, M. & Heeger, A. J. The Temperature Dependence of the Conductivity in the Critical Regime of the Metal-Insulator Transition in Conducting Polymers. *J. Phys.: Condens. Matter* **9**, 4145–4156 (1997).
3. Kaiser, A. B. Electronic Transport Properties of Conducting Polymers and Carbon Nanotubes. *Rep. Prog. Phys.* **64**, 1–49 (2001).